

Reversible Visible-Light Photooxidation of an Oxomanganese Water-Oxidation Catalyst Covalently Anchored to TiO₂ Nanoparticles[†]

Gonghu Li, Eduardo M. Sproviero, William R. McNamara, Robert C. Snoeberger III, Robert H. Crabtree,* Gary W. Brudvig,* and Victor S. Batista*

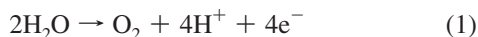
Department of Chemistry, Yale University, P.O. Box 208107, New Haven, Connecticut 06520-8107

Received: September 15, 2009; Revised Manuscript Received: October 16, 2009

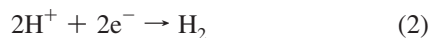
Several polynuclear transition-metal complexes, including our own dinuclear di- μ -oxo manganese compound [H₂O(terpy)Mn^{III}(μ -O)₂Mn^{IV}(terpy)H₂O](NO₃)₃ (**1**, terpy = 2,2':6',2''-terpyridine), have been reported to be homogeneous catalysts for water oxidation. This paper reports the covalent attachment of **1** onto nanoparticulate TiO₂ surfaces using a robust chromophoric linker **L**. **L**, a phenylterpy ligand attached to a 3-phenyl-acetylacetonate anchoring moiety via an amide bond, absorbs visible light and leads to photoinduced interfacial electron transfer into the TiO₂ conduction band. We characterize the electronic and structural properties of the **1**–**L**–TiO₂ assemblies by using a combination of methods, including computational modeling and UV–visible, IR, and EPR spectroscopies. We show that the Mn(III,IV) state of **1** can be reversibly advanced to the Mn(IV,IV) state by visible-light photoexcitation of **1**–**L**–TiO₂ nanoparticles (NPs) and recombines back to the Mn(III,IV) state in the dark, in the absence of electron scavengers. Our findings also indicate that a high degree of crystallinity of the TiO₂ NPs is essential for promoting photooxidation of the adsorbates by photoinduced charge separation when the TiO₂ NPs serve as electron acceptors in artificial photosynthetic assemblies. The reported results are particularly relevant to the development of photocatalytic devices for oxidation chemistry based on inexpensive materials (e.g., TiO₂ and Mn complexes) that are robust under aqueous and oxidative conditions.

1. Introduction

The development of inexpensive photocatalytic materials for solar light-powered water oxidation would allow the sustainable production of green chemical fuel (H₂) from water. This has been a long-standing goal of photoelectrochemistry research since the first report of water photolysis on TiO₂ electrodes more than three decades ago.¹ The outstanding challenge is the design and assembly of molecular components that could efficiently absorb visible light and transfer the harvested energy to catalytic complexes for water oxidation into O₂, protons, and electrons, as in eq 1.²



The protons and electrons extracted from water could then react to produce H₂, as in eq 2.



The resulting process would mimic natural photosynthesis where light is converted into chemical fuel by coupling photosensitizers with water-oxidation catalysts.^{3–5} This paper reports the functionalization of TiO₂ nanoparticles (NPs) with a water-oxidation catalyst, [H₂O(terpy)Mn^{III}(μ -O)₂Mn^{IV}(terpy)H₂O](NO₃)₃ (**1**, terpy = 2,2':6',2''-terpyridine), using light-harvesting organic linkers that are robust to aqueous and oxidative conditions. The results

are particularly relevant to the development of photocatalytic devices for oxidation chemistry because **1** is a strong oxidant when advanced to the Mn(IV,IV) state and TiO₂ NPs are excellent electron acceptors⁶ as extensively applied in dye-sensitized solar cells.⁷ Nanoparticulate TiO₂ materials are promising building blocks for artificial synthetic assemblies largely due to the fact that TiO₂ NPs can form robust nanoporous thin films and that the electrons in the TiO₂ conduction band are capable of reducing protons to H₂.^{8,9}

Transition-metal complexes are known for their capacity to store multiple redox equivalents and to catalyze high-energy, small-molecule reactions such as water oxidation or CO₂ reduction.^{10,11} A variety of homogeneous^{12,13} and heterogeneous¹⁴ water-oxidation catalysts based on transition metals have been developed, including complexes of Ru,^{15–18} Mn,^{19–24} Ir,^{25–28} and Co.^{29,30} In Nature, water oxidation is catalyzed by the Mn₄Ca inorganic unit embedded in the D1 protein subunit of photosystem II.^{31,32} In recent studies, we have focused on the structure of the Mn₄Ca complex and on the catalytic mechanism of multielectron water oxidation and oxygen evolution in photosystem II at the molecular level.^{33–36} In addition, we have developed^{19–22} and analyzed³⁷ biomimetic Mn complexes, including the di- μ -oxo manganese dimer **1** that is capable of chemically oxidizing water when activated with a primary oxidant such as oxone (2KHSO₅·KHSO₄·K₂SO₄). Once coupled to electron acceptor surfaces, such complexes could accumulate redox equivalents and subsequently catalyze water oxidation. Thus, it is important to study attachment schemes for coupling these molecular catalysts to electron acceptors as artificial photosynthetic assemblies for solar water splitting. In the same vein, Mallouk, Moore, and co-workers recently prepared a water-splitting assembly by attaching a heterogeneous iridium

[†] Part of the “Michael R. Wasielewski Festschrift”.

* To whom correspondence should be addressed. E-mail: robert.crabtree@yale.edu (R.H.C.); gary.brudvig@yale.edu (G.W.B.); victor.batista@yale.edu (V.S.B.).

oxide catalyst to TiO_2 , using a derivatized $[\text{Ru}(\text{bpy})_3]^{2+}$ complex (bpy = 2,2'-bipyridine) as a chromophoric linker, and demonstrated visible-light water splitting in the presence of a small applied voltage.³⁸

By mimicking the photoinduced charge separation of natural photosynthesis, molecular and supramolecular model systems can provide important inspirations for practical solar fuel production.³⁹ Hammarström, Styring, and co-workers prepared molecular assemblies coupling Mn complexes with the $[\text{Ru}(\text{bpy})_3]^{2+}$ photosensitizer and demonstrated light-induced electron transfer in their molecular assemblies.⁴⁰ For example, they synthesized a linked donor– $[\text{Ru}(\text{bpy})_3]^{2+}$ –acceptor triad using a Mn(II,II) dimer and naphthalenediimide as the electron donor and acceptor, respectively.⁴¹ Light-induced manganese oxidation and long-lived charge separation was observed in the resulting molecular triad.⁴¹ These researchers also reported the formation of a Mn(III,IV) dimer following light-induced accumulative electron transfer from the Mn(II,II) dimer to the photooxidized Ru center using a Co^{III} complex as the electron acceptor.^{42,43}

A few studies have investigated the photochemical and catalytic properties of oxomanganese complexes immobilized on solid supports. Weare et al. synthesized a nanostructured assembly in which a di- μ -oxo manganese dimer $[(\text{bpy})_2\text{Mn}^{\text{III}}(\mu\text{-O})_2\text{Mn}^{\text{IV}}(\text{bpy})_2](\text{NO}_3)_3$ was coupled to a single Cr^{VI} charge-transfer chromophore in the channels of nanoporous silica.⁴⁴ They demonstrated that visible light-induced electron transfer from the $\text{Mn}^{\text{III}}(\mu\text{-O})_2\text{Mn}^{\text{IV}}$ core to Cr^{VI} led to the formation of $\text{Mn}^{\text{IV}}(\mu\text{-O})_2\text{Mn}^{\text{IV}}$ and Cr^{V} .⁴⁴ Yagi et al. deposited complex **1** on clay materials and observed catalytic oxygen evolution using Ce^{4+} as the single-electron oxidant.^{45–47} In recent work, we have investigated the direct deposition of complex **1** onto TiO_2 NPs, substituting one of its water ligands by the TiO_2 NP.⁴⁸ We found that **1** binds to near amorphous TiO_2 but dimerizes to form Mn(IV) tetramers on surfaces of well-crystallized TiO_2 NPs.⁴⁸ The Mn(IV) tetramers attached to TiO_2 oxidize water and form O_2 when activated with Ce^{4+} as the primary one-electron oxidant.⁴⁸

In this study, we build upon our earlier work^{48–50} by investigating whether complex **1** can be stabilized on surfaces of near-amorphous and well-crystallized TiO_2 NPs when covalently attached with linkers that form robust adsorbates even under aqueous and oxidative conditions.⁵⁰ We synthesize a derivative of complex **1** on the surfaces of TiO_2 NPs *in situ* by first attaching the precursor Mn(II) monomers to an anchoring ligand attached to TiO_2 NPs and then assembling the mixed-valent $\text{Mn}^{\text{III}}(\mu\text{-O})_2\text{Mn}^{\text{IV}}$ unit by treatment with KMnO_4 . The resulting surface complex is characterized by combining UV–visible, IR, and EPR spectroscopies with computational modeling. We observe the reversible advancement of the mixed-valent di- μ -oxo Mn(III,IV) state to the Mn(IV,IV) state by photoexcitation and interfacial electron injection into the conduction band of TiO_2 .

2. Experimental Procedures

All reagents and solvents were purchased from Aldrich and used without further purification. Milli-Q water was used to make all of the aqueous solutions.

2.1. Materials Synthesis. 2.1.1. Synthesis of TiO_2 Nanoparticles. A commercially available TiO_2 sample, Degussa P25, was used as received from Evonik. The P25 TiO_2 is well crystallized and consists of $\sim 85\%$ anatase and $\sim 15\%$ rutile (Figure S1 in the Supporting Information). Using titanium(IV) isopropoxide as the Ti precursor, a near-amorphous TiO_2 material (denoted “D70”) was synthesized in dichloromethane

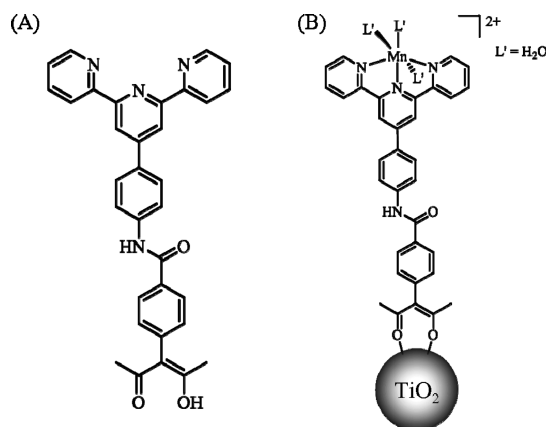


Figure 1. Structures of (A) the synthetic organic linker **L** and (B) $\text{Mn}^{\text{II}}\text{--L--TiO}_2$.

by a modified solvothermal method as previously described.⁴⁸ Further characterization shows that D70 contains the anatase phase with a relatively low degree of crystallinity (Figure S1 in the Supporting Information) and small particle sizes (Figure S2 in the Supporting Information).⁴⁸ The specific surface areas of P25 and D70 NPs were determined to be 50 and 310 m^2/g , respectively.⁴⁸

2.1.2. Sensitization of TiO_2 Nanoparticles with an Organic Linker. The synthetic organic linker **L** is a phenylterpyridine ligand attached to 3-phenyl-acetylacetonate via an amide bond (see Figure 1A) which was synthesized as previously described.⁵⁰ Surface sensitization of TiO_2 NPs was done by stirring 500 mg of TiO_2 NPs in a 50 mL solution of 1 mM **L** in dichloromethane at room temperature for 18 h.⁵⁰ The sensitized TiO_2 NPs were then washed with dichloromethane and were collected by solvent evaporation (denoted “**L**– TiO_2 ”).

2.1.3. Synthesis of the $\text{Mn}^{\text{III}}(\mu\text{-O})_2\text{Mn}^{\text{IV}}$ Complex on **L– TiO_2 .** In this study, KMnO_4 was used as the oxidant in order to assemble the mixed-valent $\text{Mn}^{\text{III}}(\mu\text{-O})_2\text{Mn}^{\text{IV}}$ complex onto TiO_2 NPs via the organic linker **L**. In a typical synthesis, 20 mg of **L**– TiO_2 was washed with water before mixing with 3 mL of 2 mM MnCl_2 . The resulting mixture was stirred at room temperature for 2 h and was then washed with water to remove the excess MnCl_2 , leading to the formation of a surface manganese complex, $\text{Mn}^{\text{II}}\text{--L--TiO}_2$ (see Figure 1B).⁵⁰ The surface complex was then mixed with 2 mL of 2 mM KMnO_4 and stirred at room temperature under dark conditions. The liquid phase extracted from the reaction mixture after 18 h remained purple, indicating KMnO_4 used in the reaction was in excess. The thus obtained functionalized TiO_2 NPs were recovered and thoroughly washed with water by centrifugation (all done under dark conditions). As discussed below, this procedure led to the formation of the mixed-valent $\text{Mn}^{\text{III}}(\mu\text{-O})_2\text{Mn}^{\text{IV}}$ complex on TiO_2 NPs via the linker **L**. The final product is denoted “**1**–**L**– TiO_2 ”.

2.1.4. Direct Deposition of **1 on TiO_2 Nanoparticles.** Following the method of Chen et al.,⁵¹ the precursor of complex **1**, $\text{Mn}^{\text{II}}(\text{terpy})\text{Cl}_2$, was obtained by reaction of terpy with an excess of MnCl_2 . To directly deposit complex **1** on TiO_2 , 2.4 μmol of $\text{Mn}^{\text{II}}(\text{terpy})\text{Cl}_2$ was mixed with 20 mg of TiO_2 in 3 mL of water before adding 1 mL of 2 mM KMnO_4 at room temperature. The resulting mixture was stirred at room temperature for 90 min before recovering and thoroughly washing the functionalized TiO_2 NPs by centrifugation. As discussed below, this procedure led to the formation of the mixed-valent $\text{Mn}^{\text{III}}(\mu\text{-O})_2\text{Mn}^{\text{IV}}$ complex on near-amorphous TiO_2 NPs. The thus functionalized TiO_2 materials are denoted “**1**– TiO_2 ”.

2.2. Materials Characterization. 2.2.1. EPR Spectroscopy.

Perpendicular-mode EPR spectra were recorded on an X-band Bruker Biospin/ELEXSYS E500 spectrometer equipped with an SHQ cavity and an Oxford ESR-900 liquid helium cryostat. All spectra were collected on water-dispersed samples in 5 mm OD quartz EPR tubes. The samples were subjected to N₂ purge and were frozen in liquid N₂ prior to recording spectra at 7 K. A Fiber-Lite Series 180 illuminator (Dolan-Jenner Industries, Inc., intensity 60 mW/cm²) equipped with a fiber optic light guide, which only transmits light with wavelengths greater than 425 nm (see Figure S3 in the Supporting Information), was used as the visible-light source in photochemical studies.

2.2.2. Infrared Spectroscopy. Attenuated total reflection (ATR) infrared spectra were recorded on a Nicolet 6700 infrared spectrometer. In ATR experiments, sensitized TiO₂ NPs were dispersed in water and deposited on a ZnSe crystal. Prior to collecting infrared spectra, the TiO₂ NPs on the ZnSe crystal were dried in air at room temperature. Typically, 128 scans were performed for each spectrum with a spectral resolution of 2 cm⁻¹.

2.2.3. UV–Visible Spectroscopy. Bare and functionalized TiO₂ NPs were dispersed in 1 mL of H₂O and transferred to microscopic slides, forming thin films after drying at room temperature. The optical spectra of thus prepared thin films were collected on a Varian Cary 3 spectrophotometer in diffuse reflectance geometry. The background spectrum of a blank microscope slide was always subtracted.

2.2.4. Elemental Analysis. The amount of linker **L** on TiO₂ NPs was measured on a Costech ECS 4010 elemental analyzer (Costech Analytical Technologies, Valencia, CA) coupled to a ThermoFinnigan DeltaPLUS Advantage stable isotope mass spectrometer (Thermo Scientific, Boca Raton, FL), with both controlled by the Thermo's Isodat 2.0 software.⁴⁸ In a typical run, a dried TiO₂ powder sample was sealed in a tin capsule and loaded into the autosampler. Control experiments were done using pure TiO₂ materials, and the results were calibrated with the house standard (standard cocoa powder, 4.15% N; 48.7% C). The output of the elemental analyzer, N₂ and CO₂ from N and C on TiO₂ surfaces, was sampled by the mass spectrometer.

3. Computational Analysis

3.1. Structural Models. Precursor structural models of TiO₂ anatase NPs were obtained by DFT geometry optimization from the crystal structure of bulk anatase (Figure S4 in the Supporting Information). Model nanoparticles, composed of compound **1** attached onto the surface (101) of TiO₂ anatase, were described by 32 [TiO₂] units with dimensions 1.0 nm × 1.5 nm × 3.1 nm along the [−101], [010], and [101] directions, respectively. Periodic boundary conditions were imposed with a vacuum spacer between slabs, making the interaction between distinct surfaces in the infinitely periodic model system negligible. The surface dangling bonds were saturated with capping hydrogen atoms, in order to quench the formation of surface states and avoid unphysical low coordination numbers. The DFT geometry relaxation was performed by using the Vienna *Ab-initio* Simulation Package (VASP/VAMP),⁵² implementing the PW91/GGA approximation in plane-wave basis ultrasoft Vanderbilt pseudopotentials to describe the ionic interactions. A wave function cutoff of 400 eV was used in all calculations as well as a single Gamma point *k*-point sampling due to the large size of the supercell. The Kohn–Sham (KS) Hamiltonian was projected onto a plane-wave basis set, and high-efficiency iterative methods were implemented to obtain the KS eigenstates and eigenvalues. Self-consistency was accelerated by means of efficient charge density mixing schemes.

Having obtained models of TiO₂ anatase NPs, we constructed structural models of **L**–TiO₂ slabs with dimensions of 32 Å × 15 Å × 6 Å composed of 105 [TiO₂] units, and two units of the linker **L** covalently attached on the 101 surface. The model slabs were capped with terminal OH fragments, and the geometry was optimized by energy minimization at the PW91/GGA level of theory, using plane-waves and ultrasoft Vanderbilt pseudopotentials as applied for the precursor structural models of bare TiO₂ NPs.

3.2. QM/MM Hybrid Models. QM/MM structural models of **1**–**L**–TiO₂ were built from the optimized **L**–TiO₂ model and the optimized geometry of compound **1** obtained by geometry optimization at the DFT/B3LYP level of theory (Figure S5 in the Supporting Information, left), using the X-ray atomic coordinates obtained from the Cambridge Crystallographic Data Center (CCDC) with reference code FIQFIU as the initial guess configuration.¹⁹ The QM layer of the DFT-QM/MM model of **1**–**L**–TiO₂ includes the Mn^{III}(μ-O)₂Mn^{IV} unit, the two water molecules ligated to Mn, the two terpyridine ligands, and the amide and phenyl groups of the linkers (see Figure 1). The rest of the system comprises the MM layer. The boundary between the QM and MM layers is defined, according to the standard link-hydrogen atom scheme implemented in Gaussian 03,⁵³ by cutting the covalent bonds linking the phenyl and acetylacetonate (acac) groups and completing the covalencies with frontier hydrogen atoms.

A combination of basis sets is applied to optimize the efficiency of DFT-QM/MM calculations. The lacvp basis set for Mn ions considers nonrelativistic electron–core potentials, the 6-31G* basis set for bridging O^{2−} ions includes polarization functions on μ-oxo bridging oxides, and the 6-31G basis set is applied to the rest of the atoms in the QM layer. Such a combination of basis sets has been validated through extensive benchmark calculations on high-valent manganese complexes.³⁷

QM/MM computations of **1**–**L**–TiO₂ could only be efficiently performed, according to the ONIOM-EE level of theory, after obtaining high-quality initial-guess states for the QM layer. These correspond to spin-electronic states of the cluster of Mn ions obtained according to the ligand field theory as implemented in Jaguar 5.5. Once the initial state was properly defined, the combined approach exploited important capabilities of ONIOM as implemented in Gaussian 03,⁵³ including both the link-hydrogen atom scheme for efficient and flexible definitions of QM layers and the possibility of modeling open-shell systems by performing unrestricted DFT (e.g., UB3LYP) calculations in a variety of spin-electronic states.

Fully relaxed DFT-QM/MM molecular structures were obtained at the ONIOM (UHF B3LYP/lacvp,6-31G(d),6-31G:UFF) level of theory by geometry optimization of the complete structural models subject to the constraint of fixed configuration of the TiO₂ surface and acac linker as obtained with the GGA plane wave optimization. A typical optimization procedure involved both the QM preparation of the initial spin-electronic state associated with the QM layer, and the subsequent QM/MM geometry relaxation. The optimization process preserves the purity of the initial state whenever the state is compatible with the geometry of the Mn cluster and the specific arrangement of ligands, and no other spin states of similar energy are found along the optimization process. The spin-electronic states obtained at this level of theory typically involve antiferromagnetic couplings between manganese centers. The couplings define broken-symmetry (BS) states, providing multiconfigurational character to the electronic states.^{54–57}

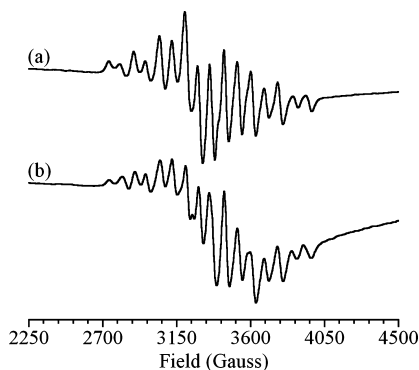


Figure 2. EPR spectra of (a) **1-L-P25** and (b) **1-L-D70**. The spectra were collected in the dark at 7 K.

4. Results and Discussion

4.1. EPR Studies of Oxomanganese Complexes on TiO₂ Surfaces. Both well-crystallized and near-amorphous TiO₂ NPs can be functionalized with the synthetic organic linker **L** by reflux in dichloromethane. We have previously demonstrated that⁵⁰ (i) functionalization with **L** effectively extends the absorption edges of TiO₂ NPs to the visible-light region, (ii) the functionalization is robust under aqueous and oxidative conditions, and (iii) ultrafast interfacial electron injection from the linker to TiO₂ occurs on a subpicosecond time scale upon visible-light excitation.

The terpy moiety in **L** (Figure 1A) allows further derivatization of TiO₂ surfaces with transition-metal complexes such as those of manganese. In order to assemble complex **1** on TiO₂ NPs through the organic linker, a surface Mn²⁺ complex (Mn^{II}-**L**-TiO₂, Figure 1B) was first prepared by stirring **L**-TiO₂ in a solution of Mn²⁺ at room temperature.⁵⁰ Further characterization indicated the coordination of Mn(II) to the terpy ligand on TiO₂ surfaces (Figure S6 in the Supporting Information). More surface Mn(II) was supported on the near-amorphous TiO₂ material (D70) than the well-crystallized P25, likely due to the relatively high surface area of D70.

In our study, Mn^{II}-**L**-TiO₂ was mixed with KMnO₄ at room temperature in order to assemble Mn^{III}(μ-O)₂Mn^{IV} units on TiO₂ through the linker **L**. The resulting materials, denoted **1-L**-TiO₂, were thoroughly washed with water and collected by centrifugation in the dark prior to measuring the EPR spectra shown in Figure 2. The characteristic 16-line EPR signal from the mixed-valent Mn(III,IV) state is seen for both **1-L**-P25 and **1-L**-D70. The 16-line EPR signal originates from the hyperfine coupling between an *S* = 1/2 electron spin and two nonequivalent ⁵⁵Mn nuclei.⁵⁸ Under the same experimental conditions, the mixture of Mn^{II}-**L**-P25 and KMnO₄ prior to washing with water was also examined with EPR spectroscopy. A 16-line EPR signal nearly identical to that shown in Figure 2a was observed, indicating the Mn^{III}(μ-O)₂Mn^{IV} units were successfully attached to the surfaces of P25 NPs.

In EPR experiments, the same amount of TiO₂ materials was always used to collect spectra under the same conditions. This allows a quantitative comparison between different samples. Although a larger number of surface Mn(II) was supported on D70 than P25 through the linker **L** (Figure S6 in the Supporting Information), the amount of Mn(III,IV) dimer **1** immobilized on D70 through **L** is slightly less than that on P25 because the 16-line EPR signal of **1-L**-P25 is more intense than **1-L**-D70 (Figure 2). It should be pointed out that some Mn(II) remained on the TiO₂ surfaces after reacting Mn^{II}-**L**-TiO₂ with KMnO₄ because a broad surface-bound Mn(II) signal centered

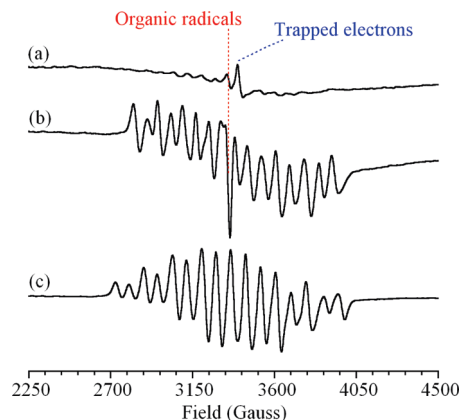


Figure 3. EPR spectra of (a) **1-P25**, (b) **1-D70**, and (c) isolated **1** in water prepared by the reaction between Mn^{II}(terpy)Cl₂ and KMnO₄. Resonances corresponding to organic radicals and Ti³⁺ (lattice-trapped electrons in TiO₂) are labeled. The spectra were collected in the dark at 7 K.

at *g* = 2.0 (see Figure S6 in the Supporting Information) was present in the EPR spectra shown in Figure 2, especially in the spectrum of **1-L**-D70. This indicates that not all of the Mn^{II}-**L**-TiO₂ was converted into **1-L**-TiO₂ by the KMnO₄ treatment.

Further EPR studies were done to confirm that the Mn^{III}(μ-O)₂Mn^{IV} units were immobilized on TiO₂ NPs via the synthetic linker **L** after the KMnO₄ treatment. The mixed-valent Mn(II-I,IV) dimer **1** was deposited directly onto the surfaces of TiO₂ NPs following an *in situ* synthesis and was investigated with EPR spectroscopy. In the *in situ* synthesis, complex **1** was prepared from its precursor, Mn^{II}(terpy)Cl₂, in the presence of TiO₂ NPs using KMnO₄ as the oxidant. On the surfaces of near-amorphous D70 NPs, complex **1** was stabilized via an oxo bridge (Mn-O-Ti), formed upon substitution of a water ligand by a TiO₂ NP (see Figure S5 in the Supporting Information, right).⁴⁸ This is clearly evidenced by the 16-line EPR spectra shown in Figure 3. The hyperfine coupling tensors for Mn^{III} and Mn^{IV} nuclei are significantly smaller for **1-D70** (Figure 3b) than isolated **1** (Figure 3c), which was synthesized by the KMnO₄ method in the absence of TiO₂ NPs. Obviously, substituting one of its water ligands by a TiO₂ NP altered the Mn^{IV} coordination environment and subsequently the hyperfine coupling tensors of complex **1**.⁴⁸

The characteristic 16-line signal is barely resolved with relatively low intensity in the EPR spectrum of **1-P25** (Figure 3a) prepared by mixing Mn^{II}(terpy)Cl₂ with KMnO₄ in the presence of P25 NPs. This implies that complex **1** containing the Mn^{III}(μ-O)₂Mn^{IV} unit cannot be directly deposited on well-crystallized P25 by substituting one water ligand with a P25 NP. The dimerization of complex **1** likely occurred on P25 NP surfaces, forming an EPR-silent Mn(IV) tetramer.⁴⁸

On the basis of the above observations, we concluded that the intense 16-line EPR signal of **1-L**-P25 shown in Figure 2a originates from Mn^{III}(μ-O)₂Mn^{IV} units immobilized on P25 NPs via the synthetic linker **L**. This is also true for **1-L**-D70 because an altered 16-line EPR signal would be seen for complex **1** directly deposited on D70 (Figure 3b). Instead, the hyperfine coupling tensors for Mn^{III} and Mn^{IV} derived from the 16-line spectrum of **1-L**-D70 (Figure 2b) are identical to those of isolated complex **1** (Figure 3c) and **1-L**-P25 (Figure 2a). This confirms that Mn^{III}(μ-O)₂Mn^{IV} units were immobilized on D70 NPs via **L**.

Comparative EPR studies and elemental analysis were done in order to estimate the amount of complex **1** attached to TiO₂

NPs through the linker **L**. In the EPR experiments, functionalized TiO₂ NPs were dispersed in H₂O, forming heterogeneous suspensions. Therefore, it was difficult to accurately quantify the amounts of Mn^{III}(μ-O)₂Mn^{IV} units in **1-L-TiO₂** samples by using a calibration curve of homogeneous complex **1**. Instead, the 16-line EPR signal of **1-L-D70** was quantitatively compared to that of **1-D70**, in which the loading of complex **1** was determined by elemental analysis to be 12 μmol/g of D70 NPs. Because the 16-line EPR signal of **1-L-D70** has similar intensity to that of **1-D70** (Figure S7 in the Supporting Information), we estimate that the loadings of complex **1** in the two samples are about the same. This implies that the loading of complex **1** in **1-L-P25** is slightly greater than 12 μmol/g of P25 NPs because the 16-line EPR signal of **1-L-P25** is more intense than **1-L-D70** (Figure 2).

The amounts of linker **L** attached to TiO₂ NPs were also determined by elemental analysis using **L-TiO₂** samples. Although D70 has a larger surface area than P25, the amounts of linker **L** on both P25 and D70 NPs were determined to be ~34 μmol/g of TiO₂. Assuming all of the linker molecules were coordinated to Mn(II) in Mn^{II}-**L-TiO₂**, the elemental analysis data suggest that ~70% of Mn^{II}-**L-TiO₂** was converted to **1-L-TiO₂** after the treatment with KMnO₄ (considering two Mn^{II}-**L** moieties are needed to assemble one **1-L** unit on TiO₂, as explained in the next paragraph). This is consistent with the EPR spectra shown in Figure 2, indicating that not all of the Mn^{II}-**L-TiO₂** was converted into **1-L-TiO₂** by the KMnO₄ treatment.

It has been shown that complex **1** containing the Mn^{III}(μ-O)₂Mn^{IV} unit can be synthesized from its precursor, Mn^{II}(terpy)Cl₂, using oxone as the oxidant.⁵¹ However, attempts to synthesize **1-L-TiO₂** by using oxone as the oxidant were unsuccessful (Figure S8 in the Supporting Information). We propose an “elbow” structure as the most probable configuration of our synthesized **1-L-TiO₂** materials (Figure 4 and section 4.2). This can explain the inability of oxone to assemble complex **1** on **L-TiO₂**. As can be seen from Figure 4, the bending of amide bonds is necessary for the assembly of one Mn^{III}(μ-O)₂Mn^{IV} unit on the TiO₂ surface through two linker molecules. Likely, the amide bonds were cleaved by hydrolysis while attempting to assemble complex **1** in the acidic oxone solutions.

4.2. Computational Analysis and Spectroscopic Studies of 1-L-TiO₂. Computational analysis and further spectroscopic studies were carried out to further investigate the “elbow” structure of **1-L-TiO₂** (Figure 4). The electronic states of the structural models, fully relaxed at the ONIOM QM/MM level of theory, involve antiferromagnetic couplings between manganese centers. The resulting optimized structures are analyzed and evaluated not only on the basis of the total energy of the system but also as compared to structural, electronic, and mechanistic features that should be consistent with experimental data. Several orientations of the ligands were analyzed. When the terpy rings are parallel to the TiO₂ surface, the terpy system suffers significant distortion. However, when they are arranged perpendicular to the surface, they keep more closely their isolated structure. The low deformation of the ligand system of **1** is confirmed by the EPR data, which show that the isolated (Figure 3c) and linked systems (Figure 2) have almost identical hyperfine coupling tensors. The linkers can be attached at two different positions, one on the same Ti-alignment plane (nonshifted configuration), attached to two Ti atoms 20.97 Å apart, and the other in two different Ti-alignment planes (shifted configuration), attached to Ti atoms 21.20 Å apart (Figure 5).

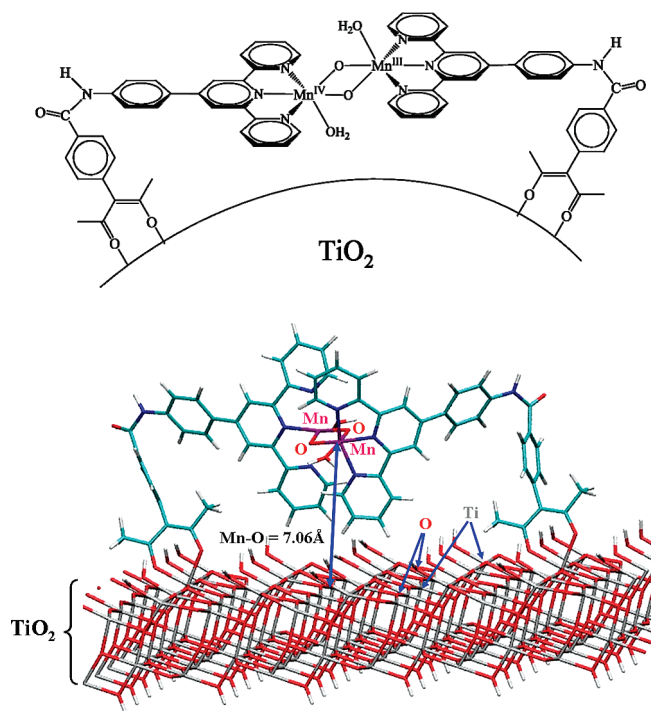


Figure 4. (top) A proposed configuration of **1-L-TiO₂**. (bottom) The relaxed configuration of compound **1** and linker **L** attached onto the surface of a TiO₂ NP optimized at the DFT-QM/MM level. Atoms in the surface complex are represented by sticks of different colors: H (silver), O (red), N (blue), C (light green), Mn (purple).

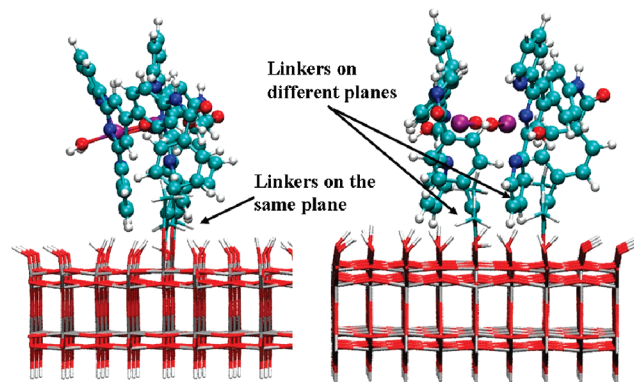


Figure 5. Transverse point of view (left, nonshifted; right, shifted) of the relaxed configuration of complex **1** and linker **L** attached onto the surface of a TiO₂ NP (see Figure 4). Atoms in the surface complex are represented by spheres of different colors and sizes: H (silver), O (red), N (blue), C (light green), Mn (purple). The QM region is depicted as balls and sticks and the MM region as sticks.

QM/MM energetic analysis shows that the energy difference between both configurations is less than 1 kcal/mol.

The structural and electronic analysis of our QM and DFT-QM/MM models indicate that our **1-L-TiO₂** assembly likely has the nonshifted configuration. As can be seen from the calculated data listed in Table 1, the Mn-ligand distances in isolated complex **1** are very close to those in **1-L-TiO₂** having the nonshifted configuration. In the shifted configuration, the Mn^{IV}-oxo (Table 1, second row) and Mn^{IV}-N (fourth row) distances are significantly greater than the corresponding distances in isolated complex **1**; the EPR signal of this “shifted” **1-L-TiO₂** would be significantly different from that of isolated complex **1**. As discussed earlier, the hyperfine coupling tensors for Mn^{III} and Mn^{IV} derived from the 16-line spectrum of **1-L-TiO₂** (Figure 2) are identical to those of isolated complex

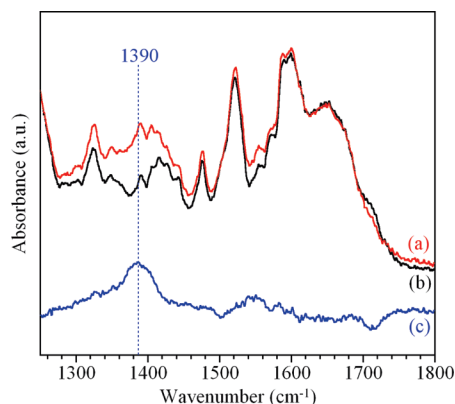
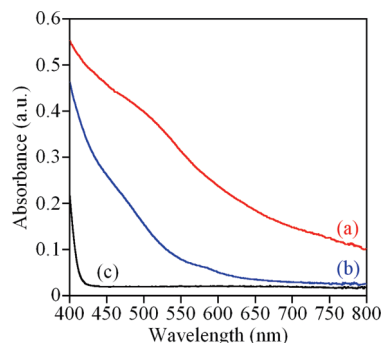
TABLE 1: Calculated Mn–Ligand Distances of Isolated Complex 1, 1–TiO₂, and 1–L–TiO₂

atom pair	atom–atom distance (Å)			
	complex 1	1–TiO ₂	1–L–TiO ₂	
			nonshifted	shifted
Mn ^{III} –Oxo	1.83, 1.91	1.82, 1.82	1.84, 1.91	1.81, 1.83
Mn ^{IV} –Oxo	1.73, 1.77	1.77, 1.84, 1.82	1.75, 1.76	1.81, 1.82
Mn ^{III} –N	2.06, 2.21, 2.21	2.19, 2.28, 2.41	2.04, 2.21, 2.33	2.15, 2.27, 2.42
Mn ^{IV} –N	2.00, 2.03, 2.03	2.02, 2.06, 2.06	2.03, 1.99, 2.05	2.26, 2.15, 2.33
Mn ^{III} –OH ₂	2.22	2.11	2.15	2.12
Mn ^{IV} –OH ₂	2.15		2.10	2.15

1 (Figure 3c). Therefore, the nonshifted configuration (Figure 5, left) represents a better description of our **1–L–TiO₂** assembly. In addition, the nonshifted configuration causes negligible variation to the spin densities of the Mn centers; the calculated values change from 3.83 au (Mn^{III}) and 2.57 au (Mn^{IV}) for isolated compound **1** to 3.84 au (Mn^{III}) and 2.61 au (Mn^{IV}) in nonshifted **1–L–TiO₂**, respectively. The corresponding values were calculated to be 3.81 au (Mn^{III}) and 2.81 au (Mn^{IV}) for the shifted configuration.

The attachment of **1** directly to TiO₂ NPs does not significantly affect the spin density of the Mn centers; the spin densities are estimated to be 3.88 au (Mn^{III}) and 2.53 au (Mn^{IV}).⁴⁸ Structural rearrangements are more significant in **1–L–TiO₂**. For example, one of the terpy ligands exhibits a slight distortion upon immobilization of complex **1** on TiO₂, leading to a pronounced increase in the Mn^{III}–N distances (Table 1, third row). By comparison with the isolated form of complex **1**, the direct attachment of the complex to the TiO₂ surface relaxes the Mn^{IV}–(μ-oxo) distances (Table 1, second row) and stabilizes the Mn^{IV} center.⁴⁸ The resulting structural rearrangements lead to a distorted 16-line EPR spectrum of **1–D70** with altered hyperfine coupling tensors (Figure 3b).

Characterization with ATR-IR spectroscopy also supports the “elbow” structure. In ATR experiments, the infrared spectra of Mn^{II}–L–P25 before and after KMnO₄ treatment were taken at room temperature. The ATR-IR spectra and the corresponding difference spectra obtained are presented in Figure 6. As can be seen from the difference spectra, a broad absorption around 1390 cm^{−1} appeared after treating Mn^{II}–L–P25 with a solution of KMnO₄. Because the amide bonds in Mn^{II}–L–P25 (Figure 1B) and **1–L–P25** (Figure 4) have *trans* and *cis* configurations, respectively, we obtained simulated IR spectra of diphenyl

**Figure 6.** ATR-IR spectra of (a) **1–L–P25** and (b) Mn^{II}–L–P25. Spectrum c shows the difference between spectra a and b.**Figure 7.** UV–visible spectra of (a) **1–L–P25**, (b) Mn^{II}–L–P25, and (c) bare P25 NPs.

amides to show spectroscopic differences between the two configurations. In the simulated IR spectra (Figure S9 in the Supporting Information), the absorption peak featuring N–H stretching between 1350 and 1400 cm^{−1} becomes much more intense when the diphenyl amide molecule changes from the *trans* configuration to *cis*. Thus, we attribute the appearance of the absorption around 1390 cm^{−1} (N–H stretching) in the difference spectrum (Figure 6c) to the formation of the “elbow” amide bond in a *cis* configuration in **1–L–P25**.

The optical absorption features of surface Mn complexes after drying at room temperature are shown in Figure 7. While bare P25 does not absorb much visible light (Figure 7c), functionalized Mn^{II}–L–P25 has significant absorption between 400 and 650 nm (Figure 7b). After treating Mn^{II}–L–P25 with KMnO₄, the resulting **1–L–P25** has a broad absorption in the visible-light region, as shown in Figure 7a. This broad absorption contains contribution from the Mn^{III}(μ-O)₂Mn^{IV} core (around 550 and 650 nm).⁵¹

4.3. Photochemical Properties of Oxomanganese Complexes on TiO₂ Surfaces. The photochemical behavior of **1–L–TiO₂** materials was studied with low-temperature EPR spectroscopy. In photochemical studies, EPR spectra were collected in the dark and under illumination with visible light having wavelengths greater than 425 nm. Difference spectra were obtained by subtracting the dark spectra from the corresponding ones under light. Upon visible-light illumination, the intensity of 16-line EPR signals characteristic of Mn^{III}(μ-O)₂Mn^{IV} units in **1–L–TiO₂** decreased significantly. As can be seen from the difference spectra shown in Figure 8A, the decrease in the 16-line signal intensity was observed for both **1–L–P25** and **1–L–D70**. Quantitative analysis indicates the intensities of 16-line EPR signals decreased by 19 and 7% for **1–L–P25** and **1–L–D70** within 1 min, respectively. Prolonged visible-light irradiation at 7 K did not cause any further change in the 16-line EPR signals.

A light-minus-dark difference EPR spectrum was also obtained for **1–D70** under the same experimental conditions. No appreciable change of the 16-line EPR signal of **1–D70** (see Figure 3b) was observed under visible-light illumination. Therefore, we conclude that the 19% change in the EPR signal of **1–L–P25** is due to the oxidation of the Mn(III,IV) state to the Mn(IV,IV) state upon visible-light irradiation. The photooxidation of Mn^{II}–L–P25 to Mn^{III}–L–P25 has been previously investigated.⁵⁰ In Mn^{II}–L–P25, the photooxidation was initiated by photoexcited charge separation in **L** followed by the oxidation of Mn(II) and electron injection into P25 NPs.⁵⁰ The visible-light oxidation of Mn^{III}(μ-O)₂Mn^{IV} to Mn^{IV}(μ-O)₂Mn^{IV} in **1–L–P25** likely followed the same mechanism. A dynamic equilibrium may exist between the Mn(III,IV) and Mn(IV,IV)

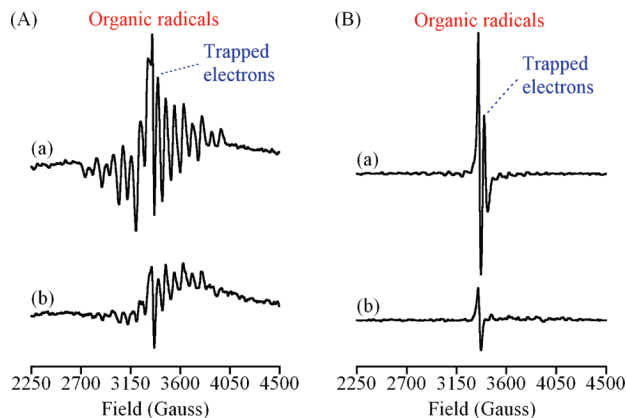
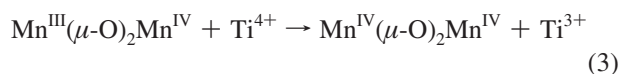


Figure 8. Difference EPR spectra of (a) **1-L-P25** and (b) **1-L-D70**. Left panel (A): light-*minus*-dark EPR spectra. Right panel (B): post-illumination dark *minus* pre-illumination dark EPR spectra. Resonances corresponding to organic radicals and TiO₂ lattice-trapped electrons (Ti³⁺) are labeled. The spectra were collected at 7 K.

states in **1-L-P25** under visible light and can explain the observation that prolonged illumination at 7 K did not cause further change in the 16-line EPR signal of **1-L-P25**. In the dynamic equilibrium, photoinduced charge separation competes with charge recombination, resulting in a steady-state concentration of Mn^{IV}(μ-O)₂Mn^{IV} (~19% on P25, assuming no Mn(IV,IV) state was formed during the KMnO₄ treatment).

Visible-light illumination also led to the formation of organic radicals in both **1-L-P25** and **1-L-D70**, as indicated by the corresponding EPR signals shown in Figure 8. An EPR signal characteristic of Ti³⁺ (TiO₂ lattice-trapped electrons) can also be resolved from the spectrum of **1-L-P25**. Equation 3 summarizes the changes shown in the light-*minus*-dark difference EPR spectrum of **1-L-P25**, including the decrease in the 16-line signal and the formation of a Ti³⁺ signal.



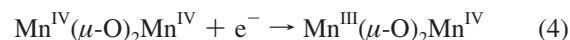
Unlike the 16-line EPR signal, both the organic radical and the trapped electron signals in the EPR spectrum of **1-L-P25** kept increasing with prolonged irradiation until reaching maximal intensities after 15 min. No lattice-trapped electron signal was seen in the difference spectrum **1-L-D70** (Figure 8b). This is consistent with the near-amorphous nature of D70 NPs (Figure S1 in the Supporting Information), in which electrons are preferentially trapped in surface defect sites and are associated with a broad EPR signal much less intense than the lattice-trapped Ti³⁺ signal.⁵⁹

Further EPR studies show that the photooxidation of Mn^{III}(μ-O)₂Mn^{IV} in **1-L-TiO₂** is completely reversible at 7 K. After illuminating the samples in the EPR cavity for 15 min, the light was turned off to allow dark recovery and subsequent collection of post-illumination dark EPR spectra. Difference spectra shown in Figure 8B were obtained by subtracting the pre-illumination dark spectra from the corresponding post-illumination dark spectra. The difference spectra shown in Figure 8B suggest a negligible change in the 16-line EPR signals, indicating that the photooxidation of Mn^{III}(μ-O)₂Mn^{IV} units in **1-L-TiO₂** is reversible.

On near-amorphous D70 NPs, the steady-state concentration of Mn^{IV}(μ-O)₂Mn^{IV} was determined to be 7%, in contrast with 19% on well-crystallized P25. This comparison highlights the

role of crystallinity of TiO₂ materials in promoting the photo-induced charge separation and inhibiting charge recombination in our synthesized **1-L-TiO₂** assemblies. In crystalline TiO₂ materials such as P25, deep traps (e.g., lattice Ti⁴⁺) allow effective electron trapping (Ti⁴⁺ + e⁻ → Ti³⁺).⁸ In near-amorphous TiO₂ NPs such as D70, the vast amount of surface defects provides abundant shallow trapping sites for electrons. However, electrons in these shallow surface traps have much shorter lifetimes than in the lattice trapping sites.⁶⁰ In our study, Ti⁴⁺ sites in P25 lattices enabled effective electron trapping, which in turn promoted charge separation in **1-L-P25**. Because the photogenerated electrons were more effectively trapped in P25 than in D70, a higher steady-state concentration of Mn^{IV}(μ-O)₂Mn^{IV} was achieved in **1-L-P25** than in **1-L-D70** (Figure 8A).

The two sharp signals corresponding to organic radicals and trapped electrons in the EPR spectra of **1-L-P25** (Figure 8a) were also observed in the light-*minus*-dark difference spectrum of **L-P25** (Figure S10 in the Supporting Information). Therefore, a significant portion of the organic radicals and the trapped electrons in **1-L-P25** originated from charge separation involving free linker molecules that did not assemble a Mn(III,IV) dimer after the KMnO₄ treatment (~30% according to elemental analysis data). Because of the existence of such “free” light-harvesting linker molecules, the source of the electrons for the dark-recovery mechanism of the 16-line EPR signal of **1-L-P25** (eq 4) is unclear based on the EPR results.



In addition to dark recovery of the Mn(III,IV) species by charge recombination of Mn^{IV}(μ-O)₂Mn^{IV} and trapped lattice electrons, it is possible that some of the Mn^{IV}(μ-O)₂Mn^{IV} units in **1-L-P25** were reduced to the Mn(III,IV) state by oxidizing free linker molecules, which would account for the increase in the EPR signal from organic radicals and some dark-stable electrons trapped in the lattice sites on P25 NPs after the visible-light illumination was turned off. In **1-L-D70**, the surface-trapped electrons recombined with Mn^{IV}(μ-O)₂Mn^{IV} in the dark, leading to the complete recovery of the 16-line EPR signal of Mn^{III}(μ-O)₂Mn^{IV}.

5. Conclusions

We have successfully assembled the **1-L-TiO₂** system based on our own water-oxidation catalyst [H₂O(terpy)Mn^{III}(μ-O)₂Mn^{IV}(terpy)H₂O](NO₃)₃ (**1**, terpy = 2,2':6',2''-terpyridine) attached to TiO₂ nanoparticles by using a synthetic organic linker **L** that consists of a phenylterpyridine ligand attached to 3-phenyl-acetylacetonate via an amide bond. The three components of the resulting molecular assembly, including **1**, **L**, and TiO₂, serve as the electron donor, the light-harvesting chromophoric linker, and the electron acceptor, respectively. To the best of our knowledge, the reported results demonstrate for the first time the feasibility of covalently attaching a high-valent oxomanganese water-oxidation catalyst to TiO₂ as well as the feasibility of reversibly advancing its oxidation state by photoexcitation with visible light. These findings are particularly relevant to the development of photocatalytic assemblies for oxidation chemistry based on inexpensive materials (e.g., TiO₂ and Mn complexes) that are robust under aqueous and oxidative conditions.

We have demonstrated that the mixed-valent Mn(III,IV) state of the water-oxidation catalyst **1** is readily formed upon KMnO₄

treatment of TiO₂ NPs functionalized with Mn(II) precursor monomers, as spectroscopically manifested by the characteristic 16-line EPR signal of the Mn^{III}(μ-O)₂Mn^{IV} inorganic core and the appearance of the 1390 cm⁻¹ (N–H stretching) band in the ATR-IR spectrum, supporting the “elbow” structure predicted by our computational models. These spectroscopic and computational results indicate that the resulting immobilization of the oxomanganese catalysts on TiO₂ NPs require negligible structural and electronic rearrangements of the water-oxidation catalyst.

Consistent with our earlier study of TiO₂ NPs functionalized with the precursor Mn(II) monomer,⁵⁰ we conclude that the functionalization of TiO₂ surfaces by covalent attachment of the Mn dimer is robust under aqueous and oxidative conditions. In fact, the resulting 1–L–TiO₂ NPs are thoroughly washed with water by centrifugation, after treatment with KMnO₄ for 18 h, before spectroscopic examination.

We conclude that the oxidation state of the Mn^{III}(μ-O)₂Mn^{IV} inorganic core in 1–L–TiO₂ can be advanced to the Mn^{IV}(μ-O)₂Mn^{IV} state by photoactivation with visible light, as manifested by the light-minus-dark EPR difference spectrum. These results are consistent with our earlier study of the precursor Mn(II) monomer,⁵⁰ where we demonstrated that the oxidation state of the Mn(II) center can be advanced to the Mn(III) state by visible-light excitation, leading to ultrafast interfacial electron injection from the linker to TiO₂.

Finally, we showed that visible-light oxidation of the mixed-valent Mn(III,IV) catalyst led to a higher steady-state concentration of Mn^{IV}(μ-O)₂Mn^{IV} on well-crystallized TiO₂ than on near-amorphous TiO₂ NPs. Therefore, we conclude that a high degree of crystallinity of the TiO₂ NPs is essential for promoting photoinduced charge separation when the TiO₂ NPs serve as electron acceptors in artificial photosynthetic assemblies.

Acknowledgment. The authors acknowledge support from the Division of Chemical Sciences, Geosciences, and Biosciences, Office of Basic Energy Sciences of the U.S. Department of Energy (DE-FG02-07ER15909) and DOE supercomputer time from NERSC. NSF grant CHE-0215926 provided funds to purchase the ELEXSYS E500 EPR spectrometer and the NSF ECCS # 0404191 grant supported preliminary work. The generous donation of P25 TiO₂ by Evonik is greatly appreciated. G.L. thanks Rebecca Milot, Xiaoming Wang, Dr. Salim Derrouiche, Dr. Gerald Olack, Professor Charles Schmuttenmaer, and Professor Gary Haller for their assistance in various aspects of experiments.

Supporting Information Available: X-ray diffraction patterns and transmission electron micrographs of TiO₂ NPs; spectrum of the visible-light lamp; molecular models of the TiO₂ anatase surface and complex 1, and the structure of 1–D70; EPR spectra of Mn^{II}–L–TiO₂ before KMnO₄ treatment, 1–D70 and 1–L–D70, and Mn^{II}–L–TiO₂ after the reactions with oxone; simulated IR spectra of diphenyl amide in *cis* and *trans* configurations; light-minus-dark EPR spectrum of L–P25; Complete ref 53. This material is available free of charge via the Internet at <http://pubs.acs.org>.

References and Notes

- (1) Fujishima, A.; Honda, K. *Nature* **1972**, *238*, 37–38.
- (2) Alstrum-Acevedo, J. H.; Brennaman, M. K.; Meyer, T. J. *Inorg. Chem.* **2005**, *44*, 6802–6827.
- (3) Lubitz, W.; Reijerse, E. J.; Messinger, J. *Energy Environ. Sci.* **2008**, *1*, 15–31.
- (4) Lewis, N. S.; Nocera, D. G. *Proc. Natl. Acad. Sci.* **2006**, *103*, 15729–15735.
- (5) Bard, A. J.; Fox, M. A. *Acc. Chem. Res.* **1995**, *28*, 141–145.
- (6) Moore, G. F.; Hambourger, M.; Gervald, M.; Poluektov, O. G.; Rajh, T.; Gust, D.; Moore, T. A.; Moore, A. L. *J. Am. Chem. Soc.* **2008**, *130*, 10466–10467.
- (7) Grätzel, M. *Nature* **2001**, *414*, 338–344.
- (8) Linsebigler, A. L.; Lu, G. Q.; Yates, J. T. *Chem. Rev.* **1995**, *95*, 735–758.
- (9) Carp, O.; Huisman, C. L.; Reller, A. *Prog. Solid State Chem.* **2004**, *32*, 33–177.
- (10) Fujita, E. *Coord. Chem. Rev.* **1999**, *185–186*, 373–384.
- (11) Fujita, E.; Muckerman, J. T. *Bull. Jpn. Soc. Coord. Chem.* **2008**, *51*, 41–54.
- (12) Cady, C. W.; Crabtree, R. H.; Brudvig, G. W. *Coord. Chem. Rev.* **2008**, *252*, 444–455.
- (13) Yagi, M.; Kaneko, M. *Chem. Rev.* **2001**, *101*, 21–35.
- (14) Harriman, A.; Pickering, I. J.; Thomas, J. M.; Christensen, P. A. *J. Chem. Soc., Faraday Trans. 1* **1988**, *84*, 2795–2806.
- (15) Concepcion, J. J.; Jurss, J. W.; Templeton, J. L.; Meyer, T. J. *J. Am. Chem. Soc.* **2008**, *130*, 16462–16463.
- (16) Liu, F.; Concepcion, J. J.; Jurss, J. W.; Cardolaccia, T.; Templeton, J. L.; Meyer, T. J. *Inorg. Chem.* **2008**, *47*, 1727–1752.
- (17) Deng, Z.; Tseng, H.-W.; Zong, R.; Wang, D.; Thummel, R. *Inorg. Chem.* **2008**, *47*, 1835–1848.
- (18) Geletii, Y. V.; Botar, B.; Kogerler, P.; Hillesheim, D. A.; Musaev, D. G.; Hill, C. L. *Angew. Chem., Int. Ed.* **2008**, *47*, 3896–3899.
- (19) Limburg, J.; Vrettos, J. S.; Liable-Sands, L. M.; Rheingold, A. L.; Crabtree, R. H.; Brudvig, G. W. *Science* **1999**, *283*, 1524–1527.
- (20) Limburg, J.; Vrettos, J. S.; Chen, H. Y.; de Paula, J. C.; Crabtree, R. H.; Brudvig, G. W. *J. Am. Chem. Soc.* **2001**, *123*, 423–430.
- (21) Chen, H. Y.; Faller, J. W.; Crabtree, R. H.; Brudvig, G. W. *J. Am. Chem. Soc.* **2004**, *126*, 7345–7349.
- (22) Tagore, R.; Crabtree, R. H.; Brudvig, G. W. *Inorg. Chem.* **2008**, *47*, 1815–1823.
- (23) Beckmann, K.; Uchtenhagen, H.; Berggren, G.; Anderlund, M. F.; Thapper, A.; Messinger, J.; Styring, S.; Kurz, P. *Energy Environ. Sci.* **2008**, *1*, 668–676.
- (24) Brimblecombe, R.; Swiegers, G. F.; Dismukes, G. C.; Spiccia, L. *Angew. Chem., Int. Ed.* **2008**, *47*, 7335–7338.
- (25) McDaniel, N. D.; Coughlin, F. J.; Tinker, L. L.; Bernhard, S. *J. Am. Chem. Soc.* **2008**, *130*, 210–217.
- (26) Hoertz, P. G.; Kim, Y.-I.; Youngblood, W. J.; Mallouk, T. E. *J. Phys. Chem. B* **2007**, *111*, 6845–6856.
- (27) Nakamura, R.; Frei, H. *J. Am. Chem. Soc.* **2006**, *128*, 10668–10669.
- (28) Hull, J. F.; Balcells, D.; Blakemore, J. D.; Incarvito, C. D.; Eisenstein, O.; Brudvig, G. W.; Crabtree, R. H. *J. Am. Chem. Soc.* **2009**, *131*, 8730–8731.
- (29) Kanan, M. W.; Nocera, D. G. *Science* **2008**, *321*, 1072–1075.
- (30) Brunschwig, B. S.; Chou, M. H.; Creutz, C.; Ghosh, P.; Sutin, N. *J. Am. Chem. Soc.* **1983**, *105*, 4832–4833.
- (31) McEvoy, J. P.; Brudvig, G. W. *Chem. Rev.* **2006**, *106*, 4455–4483.
- (32) Yachandra, V. K.; Sauer, K.; Klein, M. P. *Chem. Rev.* **1996**, *96*, 2927–2950.
- (33) Sproviero, E. M.; Gascon, J. A.; McEvoy, J. P.; Brudvig, G. W.; Batista, V. S. *J. Am. Chem. Soc.* **2008**, *130*, 6728–6730.
- (34) Sproviero, E. M.; Gascon, J. A.; McEvoy, J. P.; Brudvig, G. W.; Batista, V. S. *J. Am. Chem. Soc.* **2008**, *130*, 3428–3442.
- (35) Sproviero, E. M.; Gascon, J. A.; McEvoy, J. P.; Brudvig, G. W.; Batista, V. S. *Coord. Chem. Rev.* **2008**, *252*, 395–415.
- (36) Sproviero, E. M.; McEvoy, J. P.; Gascon, J. A.; Brudvig, G. W.; Batista, V. S. *Photosynth. Res.* **2008**, *97*, 91–114.
- (37) Sproviero, E. M.; Gascon, J. A.; McEvoy, J. P.; Brudvig, G. W.; Batista, V. S. *J. Inorg. Biochem.* **2006**, *100*, 786–800.
- (38) Youngblood, W. J.; Lee, S.-H. A.; Kobayashi, Y.; Hernandez-Pagan, E. A.; Hoertz, P. G.; Moore, T. A.; Moore, A. L.; Gust, D.; Mallouk, T. E. *J. Am. Chem. Soc.* **2009**, *131*, 926–927.
- (39) Balzani, V.; Credi, A.; Venturi, M. *ChemSusChem* **2008**, *1*, 26–58.
- (40) Hammarström, L.; Styring, S. *Philos. Trans. R. Soc. London, Ser. B* **2008**, *363*, 1283–1291.
- (41) Borgström, M.; Shaikh, N.; Johansson, O.; Anderlund, M. F.; Styring, S.; Akermarck, B.; Magnuson, A.; Hammarström, L. *J. Am. Chem. Soc.* **2005**, *127*, 17504–17515.
- (42) Huang, P.; Hoegblom, J.; Anderlund, M. F.; Sun, L.; Magnuson, A.; Styring, S. *J. Inorg. Biochem.* **2004**, *98*, 733–745.
- (43) Huang, P.; Magnuson, A.; Lomoth, R.; Abrahamsson, M.; Tamm, M.; Sun, L.; van Rotterdam, B.; Park, J.; Hammarström, L.; Akermarck, B.; Styring, S. *J. Inorg. Biochem.* **2002**, *91*, 159–172.
- (44) Weare, W. W.; Pushkar, Y.; Yachandra, V. K.; Frei, H. *J. Am. Chem. Soc.* **2008**, *130*, 11355–11363.
- (45) Yagi, M.; Narita, K.; Maruyama, S.; Sone, K.; Kuwabara, T.; Shimizu, K. *Biochim. Biophys. Acta* **2007**, *1767*, 660–665.
- (46) Yagi, M.; Narita, K. *J. Am. Chem. Soc.* **2004**, *126*, 8084–8085.

- (47) Narita, K.; Kuwabara, T.; Sone, K.; Shimizu, K.-i.; Yagi, M. *J. Phys. Chem. B* **2006**, *110*, 23107–23114.
- (48) Li, G.; Sproviero, E. M.; Snoeberger, R. C., III.; Iguchi, N.; Blakemore, J. D.; Crabtree, R. H.; Brudvig, G. W.; Batista, V. S. *Energy Environ. Sci.* **2009**, *2*, 230–238.
- (49) Abuabara, S. G.; Cady, C. W.; Baxter, J. B.; Schmuttenmaer, C. A.; Crabtree, R. H.; Brudvig, G. W.; Batista, V. S. *J. Phys. Chem. C* **2007**, *111*, 11982–11990.
- (50) McNamara, W. R.; Snoeberger, R. C., III.; Li, G.; Schleicher, J. M.; Cady, C. W.; Poyatos, M.; Schmuttenmaer, C. A.; Crabtree, R. H.; Brudvig, G. W.; Batista, V. S. *J. Am. Chem. Soc.* **2008**, *130*, 14329–14338.
- (51) Chen, H. Y.; Tagore, R.; Das, S.; Incarvito, C.; Faller, J. W.; Crabtree, R. H.; Brudvig, G. W. *Inorg. Chem.* **2005**, *44*, 7661–7670.
- (52) Kresse, G.; Furthmüller, J. Vienna ab initio Simulation Package (<http://cms.mpi.univie.ac.at/vasp>).
- (53) Frisch, M. J.; et al. *Gaussian 03*, revision B.04; Gaussian, Inc.: Wallingford, CT, 2004.
- (54) Noodleman, L. *J. Chem. Phys.* **1981**, *74*, 5737–5743.
- (55) Noodleman, L.; Case, D. A. *Adv. Inorg. Chem.* **1992**, *38*, 423–470.
- (56) Noodleman, L.; Davidson, E. R. *Chem. Phys.* **1986**, *109*, 131–143.
- (57) Noodleman, L.; Deng, C. Y.; Case, D. A.; Mouesca, J. M. *Coord. Chem. Rev.* **1995**, *144*, 199–244.
- (58) Cooper, S. R.; Dismukes, G. C.; Klein, M. P.; Calvin, M. *J. Am. Chem. Soc.* **1978**, *100*, 7248–7252.
- (59) Li, G.; Dimitrijevic, N.; Chen, L.; Nichols, J.; Rajh, T.; Gray, K. A. *J. Am. Chem. Soc.* **2008**, *130*, 5402–5403.
- (60) Hoffmann, M. R.; Martin, S. T.; Choi, W. Y.; Bahnemann, D. W. *Chem. Rev.* **1995**, *95*, 69–96.

JP908925Z